

Title: Two-axis Optical MEMS Scanner
Inventors: Shorya Awatar, Klint Rose, Hoe Phong Tham

Abstract:

Two axis optical MEMS mirrors find use in many applications including raster scanning, image projection, optical networking, bio-medical imaging, etc. In all these applications micro-mirrors are employed to steer a beam of light. While successive single axis mirrors may be used to steer the beam along multiple axes, a single two-axis mirror provides a simpler, more compact and inexpensive alternative. In this document, we present a two-axis optical scanning mirror design based on a novel resonant structure that provides optimal raster scanning action. The two scanning axes are orthogonal and are designed to be highly decoupled. Furthermore, translational errors of the mirror are eliminated by using the principle of virtual pivot for cantilever beams. PZT electrodes are employed to excite the structure at the frequencies that correspond to its two desired natural vibration modes. A simple fabrication process flow allows for mass production of the device. Detailed analysis is provided to support the performance claims of the device.

Background and Prior Art

Optical mirrors have become critically important in areas of medical imaging, microvision, displays, bar code recognition etc., where beam alignment, steering and scanning is needed. MEMS technology enables miniaturization and integration of such optical mirror systems and hence offers some very promising solutions to the above applications.

A relevant example is that of Optical Coherence Tomography (OCT) based imaging of biological tissues where high speed raster scanning is required [1]. A MEMS device that can produce such raster scanning is ideally suited for biomedical imaging instruments based on OCT.

Optical mirrors may operate in static beam steering mode or in a high speed scanning mode. For high speed scanning, typically a resonant device or structure is used that operates at its natural frequencies. For either of these operations, a series of single axis mirrors may be employed [2-5] to realize multiple axis beam steering or scanning. A more compact alternative is to use a single two-axes mirror but this may lead to a relatively more complex device design and lower device performance, although it saves on the assembly, integration and packaging complexity [6-17].

The design concepts found in the literature on two-axes optical scanning mirrors can be broadly divided into three categories. The simplest design is one in which the bending and torsion of a single beam produces two transverse rotations of a mirror fixed at the end of the beam and thus generates the two scanning modes [11-12]. The obvious drawback with this design is that beam bending not only produces rotation at the beam tip, it also produces translation. This translation of the mirror is undesirable because it can alter the alignment of the light beam being reflected and hence affect the optics performance (Fig.4). Furthermore, the same structural element is responsible for both the excitation modes, bending and torsion, thus coupling the two. Although a simple design, it is not free of translational error motions and doesn't provide perfect decoupling between the two scan modes.

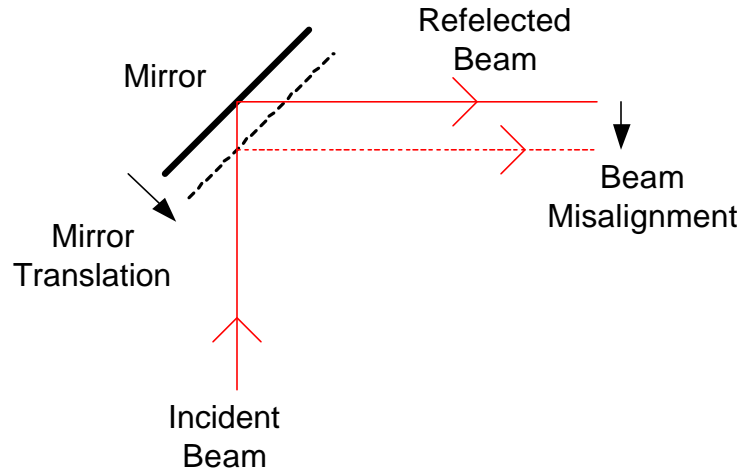
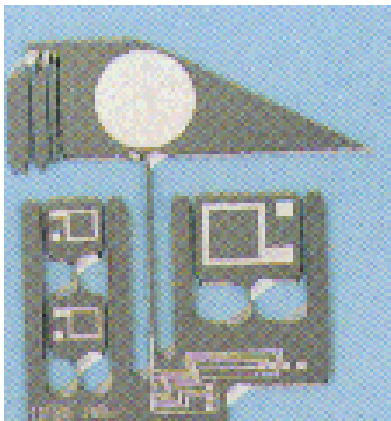


Fig.4. OMRON scanner design and its drawback

A second set of designs employ double gimbals [13-17]. These structures (Fig.5) provide perfect decoupling between the two scanning modes, but have certain other disadvantages. A double gimbals arrangement, which is an example of serial kinematics, makes actuation of the two axes a bit complex. One possible actuation method is to mount the actuator of the second axis on the moving stage of the first axis. This increases the level of complexity in fabrication. Another actuation schemes involve the use of electrostatic pads beneath the mirror. For the mirror sizes and range of motion that we are trying achieve (~1-2mm and 10-15° respectively), the gaps between the mirror and the electrostatic pads would have to be large which in turn would necessitate very high operating voltages. Other designs based on parallel kinematics like the one shown in Fig.6 make use of folded beam flexures instead of double gimbals.

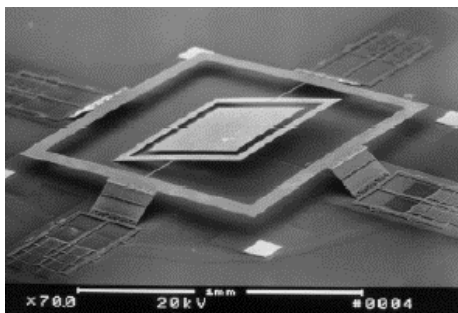


Fig. 5[16]

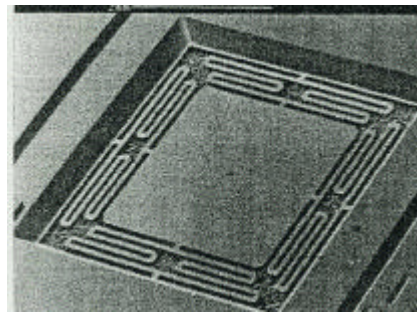


Fig. 6 [14]

The third and final group of designs is a very impressive array of 3-D self-assembled structures [17-18]. Clearly, the fabrication of these devices is a challenging process because the design involve microhinges. Furthermore packaging of these 3-D structures is a relatively complex task.

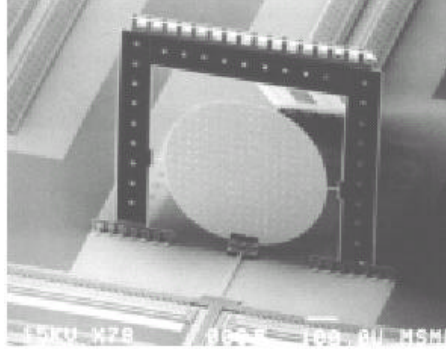


Fig. 7 [18]

In the following sections, we disclose a new two-axis MEMS scanner invention which addresses some of the key design, performance and fabrication issues. A simple design provides high performance while keeping the fabrication complexity low. The two scan axes are very well decoupled, parasitic translational errors of the mirror are eliminated, large ranges of motion are allowed, the two scan frequencies are well-separated, and the power consumption is low.

Proposed Concept

In developing our device concept we seek the fundamental objective of good design – high performance at low device complexity. We want our design to be as simple as the OMRON design mentioned above [12], and yet have decoupled and error-free motion in the two scanning modes. At the same time, it is desirable to keep the fabrication simple and hence we limit ourselves to in-plane designs.

With these factors in mind, we present a device concept illustrated in Fig. 8. An intermediate mass is supported by two cantilever beams, an assembly that is compliant in bending but stiff in torsion. The mirror itself is attached to the intermediate mass, by means of a torsion bar that is stiff in bending but compliant in torsion. Hence, one scan mode is produced by the bending of the cantilevers, during which the intermediate mass and the mirror behave like a single rigid body due to high bending stiffness of the torsion bar.

The second scanning mode arises due to the twisting of the torsion bar. If the torsional stiffness of the cantilever beams is much higher compared to the torsion bar, and if the inertia of the intermediate mass is much higher than that of the mirror, then the twisting occurs primarily in the torsion bar.

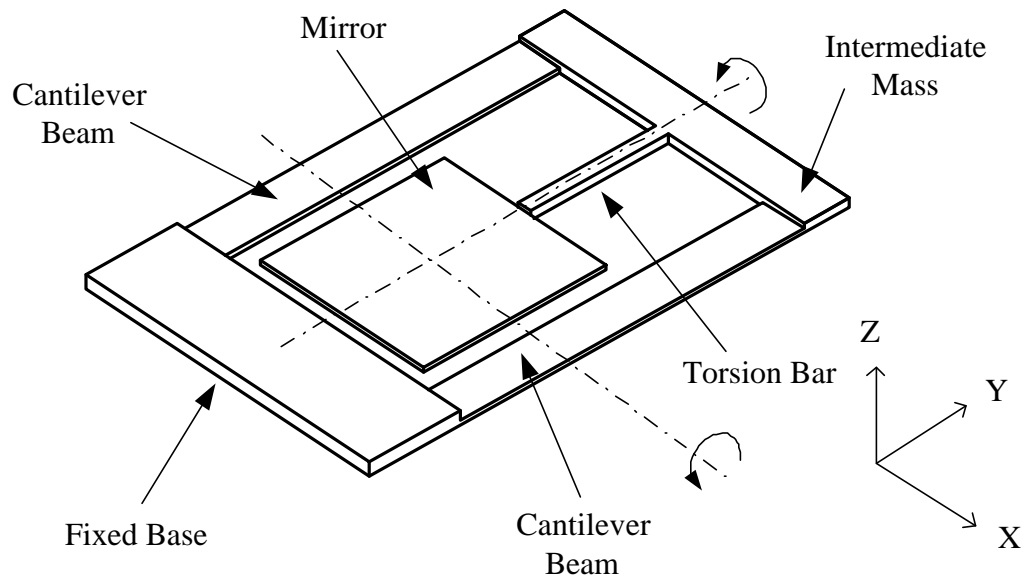


Fig. 8. Device Concept for a 2DOF scan mirror

The mirror is located with respect to the intermediate mass, such that its center axis coincides with the virtual center of rotation of the intermediate mass attached at the cantilever end. This arrangement eliminates any translation of the mirror center, as illustrated in Fig. 9. The principle of virtual center of rotation holds as long as the cantilever tips do not see any moments – either external or inertial. In a static loading case, this means that the only external load should be a force at the tip. In the case of dynamic excitation, the center of rotation shall remain stationary as long as the moment of inertia of the mass attached at the cantilever tip is low, resulting in a low inertial moment. From the subsequent dynamics analysis it shall be clear that that when the condition of zero moment of inertia of the end mass is not met, the center of rotation takes a new static position dependent on the frequency of operation.

The principle of virtual pivot for cantilever beams has been exploited by Plummer and Gonsalves in a similar mechanism for a two axis quasi-static alignment of a lens assembly, thereby achieving zero translation at the lens center.¹

¹ Bill Plummer and Tony Gonsalves, Polaroid Corp. (cited in Precision Machine Design by Alex Slocum)

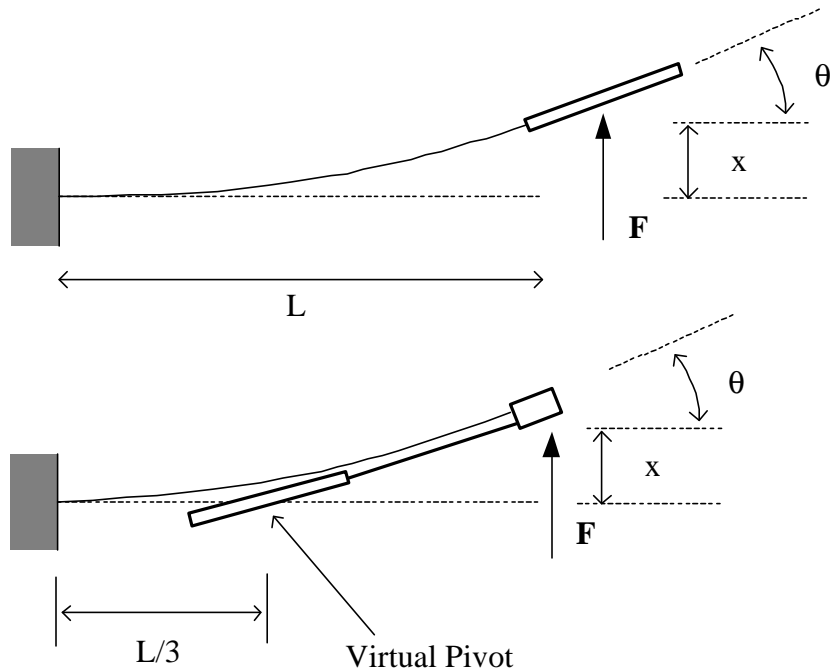


Fig. 9. Concept of Virtual Pivot for a static tip force

Being natural modes of deformation, these two correspond to the free vibrations of the structure and can be exclusively excited by actuating the structure at the right frequencies. The method or location of the actuator is not as important as the frequency of the actuation signal. Because of close-to-resonance operation, large ranges of motion can be obtained even for small actuations signals. It is hypothesized that these two modes can be excited simply by PZT actuators deposited at the base of the two cantilevers. This hypothesis is analyzed in Section 7, and is found to be a feasible option for actuation.

A number of interesting conclusions can be made here. There is no parasitic translation of the mirror which is excellent for the performance of the optical system. The two modes are physically decoupled and can be actuated independently. Bending mode is a consequence of the cantilever beams, while the torsion mode is due to the torsion bar. Furthermore, the bending natural frequency is considerably lowered due to the heavy intermediate mass. This is a very important advantage because it is desirable to have the two scan frequencies separated by at least a decade to ensure optimal scanning. The torsion frequency will still be high because of the low mirror moment of inertia.

3. Mechanical Design and Preliminary Feasibility Check

Having developed a device concept, we next proceed to perform a feasibility check to ensure that the desired natural frequencies are achievable. This is done both analytically (back of the envelope calculations) as well as using FEM. Since this initial analysis is done only to estimate the natural frequencies of the relevant modes in the structure, damping is not included. The reader is referred to Appendix A for a list of symbols.

We start with a typical mirror dimension of $1000\mu\text{m} \times 1000\mu\text{m} \times 20\mu\text{m}$. For silicon, this corresponds to a mass of $m_2 = 4.66 \times 10^{-8} \text{kg}$. Based on our previous discussion, we want our intermediate mass to be at least ten times larger. Therefore we choose the intermediate mass dimensions to be $3000\mu\text{m} \times 600\mu\text{m} \times 150\mu\text{m}$, which corresponds to $m_1 = 6.29 \times 10^{-7} \text{kg}$. The width of the intermediate mass is chosen to be large ($3000\mu\text{m}$) to ensure a large torsional stiffness of the cantilever beams. A relatively crude approximation of the first bending natural frequency is given by $\sqrt{k/(m_1 + m_2)}$, where k is the bending stiffness of the cantilevers in response to a point load. This assumes that all mass is concentrated at the cantilever tips, which clearly is an over-simplifying approximation, but is nevertheless good enough for an initial estimate. A far more detailed analysis is presented in the next section.

We choose the cantilever thickness to be $20\mu\text{m}$, since the mirror is also $20\mu\text{m}$ thick. This is done to ensure that all the features on the device have the same thickness, which in turn would make the fabrication easier. The width of the cantilevers is chosen to provide an aspect ratio of no greater than 10:1. An aspect ratio of less than this would tend to reduce the transverse bending stiffness of the cantilevers which in turn would reduce the torsional stiffness of the cantilever pair. Recalling from our discussion in Section 2, we want the torsional stiffness of the cantilever pair to be quite high. The length of the cantilevers is chosen so as to achieve a natural frequency of about 500 Hz. Thus the dimensions chosen for each cantilever are $2250\mu\text{m} \times 200\mu\text{m} \times 20\mu\text{m}$. This results in a cantilever bending stiffness value of

$$k = \frac{3EI}{L^3} = \frac{E(2w)t^3}{12L^3} = 9.4 \text{ N/m}$$

Based on this calculation, an estimate of the first natural frequency is found to be

$$w_{\text{bending}} = \sqrt{\frac{3EI}{(m_1 + m_2)L^3}} = 593 \text{ Hz} \quad (1)$$

This is within our desirable range. Next we proceed to design the torsion bar. Length of the torsion bar is decided by the length of the cantilever beams, size of the mirror and the fact that the mirror center axis should coincide with the virtual pivot of the intermediate mass, as was explained in the previous section. At this point we assume that the virtual pivot is located at a distance of one third the cantilever length from the base. We shall explain at a later stage how this fact is altered by the dynamics of the system.

These constraints require the torsion bar length to be $870\mu\text{m}$. Furthermore, we would like the torsion bar to be at least ten times stiffer in bending as compared to the cantilever beams.

Another fact to recall is that we want to maximize the bending stiffness of the rod while keeping its torsional stiffness as low as possible; this implies that a square cross-section should be ideal for the torsion bar. With these considerations, we can obtain the following results

$$\begin{aligned} \frac{w_2 t_2^3}{L_2^3} &\geq 10 \frac{(2w)t^3}{L^3} \\ \Rightarrow t_2^4 &\geq 10 \frac{(2w)t^3 L_2^3}{L^3} \\ \Rightarrow t_2 &\geq 37 \mu\text{m} \end{aligned}$$

Based on the above estimate we choose the thickness of the torsion bar to be 50 μm . Hence the torsion bar dimensions are 870 μm x 50 μm x 50 μm . These dimensions make the torsion bar about 30 times stiffer in bending as compared to the cantilever beams. With these dimensions we try to obtain an estimate for the frequency of the desired torsion mode. Once again we make some simplifying assumptions: inertia of the intermediate mass is much higher than that of the mirror, and torsional stiffness of the bar is much lower than that of the cantilevers. In that case, the torsion mode natural frequency is approximately given by $\sqrt{K_2/I_2'}$, where K_2 is the torsional stiffness of the torsion bar and I_2' is the moment of inertia of the mirror. This results in a torsion mode frequency of 16.3 kHz. This frequency is about 30 times higher than the bending mode frequency and is therefore very desirable.

The device dimensions chosen in the above basic analysis are then used to perform a finite element based modal analysis for the structure. The results are encouragingly close to the predictions made above. These dimensions then provide the starting point for subsequent iterations. But to be able to proceed with these iterations, it is important for us to have a sound analytical model, without which it will be impossible to obtain any physical insight into the dynamics of the structure. We therefore present a thorough dynamic system analysis in the next section. Detailed Finite Element Analysis (FEA) results are presented in Section 6.

4. Dynamic System Analysis

We now proceed to carry out a detailed analysis to predict the various modes and corresponding natural frequencies of the system, the quality factors associated with each mode and finally the range of motion that is obtained in close-to resonance operation. Once again, *the reader is referred to Appendix A for a list of symbols used in this section.*

We shall try to capture the bending and the torsional mode in separate lumped parameter models. For the bending analysis, we work with the assumption that the torsional bar is very stiff in bending. In the previous section, we have already seen that the bending stiffness ratio between the torsion bar and the cantilever beams is of the order of 30; therefore, this assumption is justifiable.

Hence in this model, the intermediate mass (m_1) and the mirror (m_2) are rigidly connected by the torsion bar and are treated as a single mass m with center of gravity at C . x_1 is the displacement and θ_1 is the angle of the cantilever tip. I_1^O and I_1^C are the moments of inertia of the overall mass m about points O and C respectively.

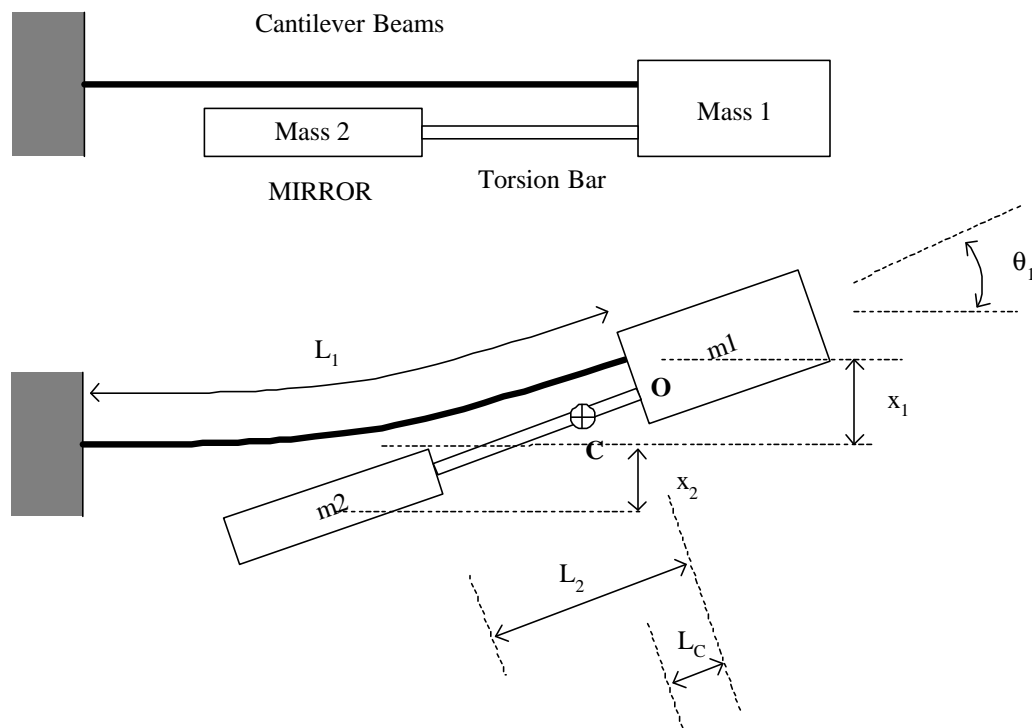


Fig. 10 The structure in its undeformed and deformed configurations.

The only two independent generalized coordinates in this model are x_1 and θ_1 . All other translations and rotations can be expressed in terms of these two coordinates. In a mechanical sense, this is a second order model and it shall predict only two bending modes. In the systems terminology, this is a fourth order model because of the four system states – two displacements

and two corresponding velocities. The first mode is expected to be simple cantilever bending mode as shown in Fig. 11 (b). The second mode occurs at high frequencies where the moment of inertia of the mass becomes the dominant inertial quantity in the system. This second bending mode is also illustrated in Fig. 11(b). This mode would not appear if we were dealing with a point mass, which is clearly not the case here. We shall elaborate this point in the subsequent analysis.

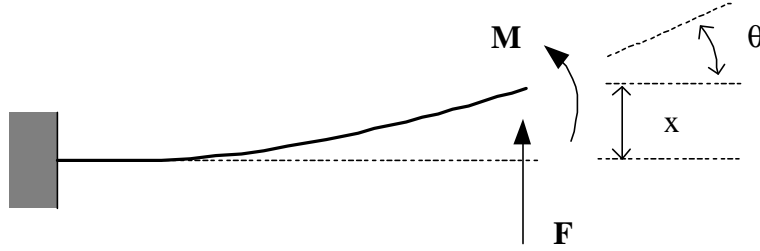


Fig. 11(a). Force-displacement of a cantilever

The generalized stiffness matrix for a cantilever is given by:

$$\begin{bmatrix} F \\ M \end{bmatrix} = \frac{12EI}{l^3} \begin{bmatrix} 1 & -\frac{l}{2} \\ -\frac{l}{2} & \frac{l^2}{3} \end{bmatrix} \begin{bmatrix} x \\ \mathbf{q} \end{bmatrix} \quad (2)$$

where the forces and displacements are as shown in Fig. 11(a).

For the cantilevers in our design, we define the quantity $\frac{12EI_1}{L_1^3} \triangleq k_1$

Using equation (2), if we draw the free body diagram of the overall mass m and apply Newton's law, we obtain the following equations of motion for the system

$$m(\ddot{x}_1 - L_c \ddot{\mathbf{q}}_1) + b_1(\dot{x}_1 - L_c \dot{\mathbf{q}}_1) = -k_1(x_1 - x_0) + \frac{k_1 L_1}{2}(\mathbf{q}_1 - \mathbf{q}_0) \quad (3)$$

$$I_1^o \ddot{\mathbf{q}}_1 = \frac{k_1 L_1}{2}(x_1 - x_0) - \frac{k_1 L_1^2}{3}(\mathbf{q}_1 - \mathbf{q}_0) + m L_c \ddot{x}_1 + b_1 L_c \dot{x}_1 - (b_2 + b_1 L_c^2) \dot{\mathbf{q}}_1 \quad (4)$$

The values for damping b_1 and b_2 are derived separately in Section 7, which presents a detailed model for viscous damping experienced by the structure. x_0 and θ_0 are initial deformations arising due to the PZT actuation at the base of the beams. A thorough discussion on this actuation scheme is presented in Section 8. From this analysis we get the following relationships,

$$\begin{aligned} \mathbf{q}_o &= c_1 V_{in} \\ x_o &= L_1 c_1 V_{in} \end{aligned} \quad (5)$$

Making these substitutions and taking Laplace transforms in equations (3) and (4),

$$\begin{aligned} (ms^2 + b_1s + k_1) X_1 &= (mL_c s^2 + b_1L_c s + \frac{k_1L_1}{2}) \Theta_1 + \frac{k_1L_1c_1}{2} V_{in} \\ [I_1^o s^2 + (b_2 + b_1L_c^2)s + \frac{k_1L_1^2}{3}] \Theta_1 &= (mL_c s^2 + b_1L_c s + \frac{k_1L_1}{2}) X_1 - \frac{k_1L_1^2c_1}{6} V_{in} \end{aligned} \quad (6)$$

Eliminating X_1 from the above two linear equations we obtain

$$\begin{aligned} &\left[mI_1^c s^4 + (mb_2 + I_1^c b_1)s^3 + \left\{ mk_1L_1 \left(\frac{L_1}{3} - L_c \right) + k_1I_1^o + b_1b_2 \right\} s^2 \dots \right. \\ &\quad \left. \dots \left\{ b_1k_1L_1 \left(\frac{L_1}{3} - L_c \right) + b_1k_1L_c^2 + b_2k_1 \right\} s + \frac{k_1^2L_1^2}{12} \right] \Theta_1 \\ &= \left[m \left(L_c - \frac{L_1}{3} \right) s^2 + b_1 \left(L_c - \frac{L_1}{3} \right) s + \frac{k_1L_1}{6} \right] \frac{k_1L_1c_1}{2} V_{in} \end{aligned} \quad (7)$$

The coefficient of Θ_1 in the above expression is the characteristic polynomial of this system model. Since the characteristic polynomial has an order 4, it represents two resonance bending modes, or two modes of free vibration. The first mode which occurs at a low frequency corresponds to simple bending while the second mode, which is a high frequency mode, arises due to moment of inertia of mass m . These two bending modes are illustrated in Fig 11 (b).

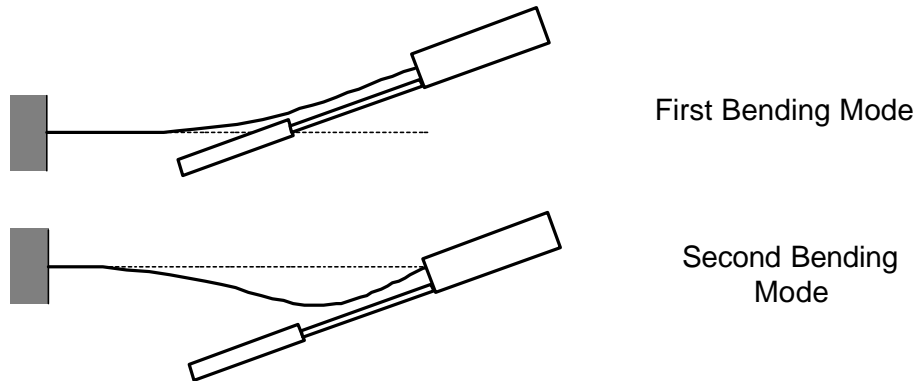


Fig. 11(b) Beam bending modes

In the first mode, the two states θ and x are in phase with each other and are related algebraically. This can be deduced by closely examining equation (6). If we choose a system that has a small L_c and moment of inertia, we can say that the mass at the end can be closely approximated by a point mass. In that case, for the low frequency resonance the term $I_1^0 s^2$ will be negligibly small. Also, at the resonance input V_{in} to the system is very small. Hence the second equation in (6) reduces to an algebraic relation between x_1 and θ_1 , whereas the first equation reduces to a simplified dynamic equation which predicts a natural frequency of $\sqrt{\frac{k_1}{4m}} = \sqrt{\frac{3EI_1}{mL_1^3}}$. This exactly the same as the approximately expression (1) that we used in

Section 3. These qualitative statements have been verified by using actual numbers and generating numerical results in MATLAB. The second bending mode arises at large frequencies when the moment of inertia of the mass m becomes an important consideration. Also it can be deduced that as the excitation frequency increases the virtual pivot of rotation of mass m moves from a location one third of the cantilever length from the base, to the cantilever tip. Hence in the first mode, the virtual pivot is close to the one-third length location while in the second mode, the virtual pivot is almost at the cantilever tip. This is evident from Fig. 11(b).

Of course there are subsequent bending modes arising from the bending of the torsion bar, but to keep the analysis tractable we are limiting ourselves to this level of complexity and it serves our purpose very extremely well. A higher order model was also developed, which includes the bending compliance of the torsion bar, but is not presented here for the sake of brevity.

A similar dynamics analysis is carried out to model the torsion modes. In this case, once again, we have two generalized coordinates ϕ_1 and ϕ_2 . This model shall predict two torsion modes of the system; it is the second torsion mode that we are interested in. A physical model is presented in Fig. 12.

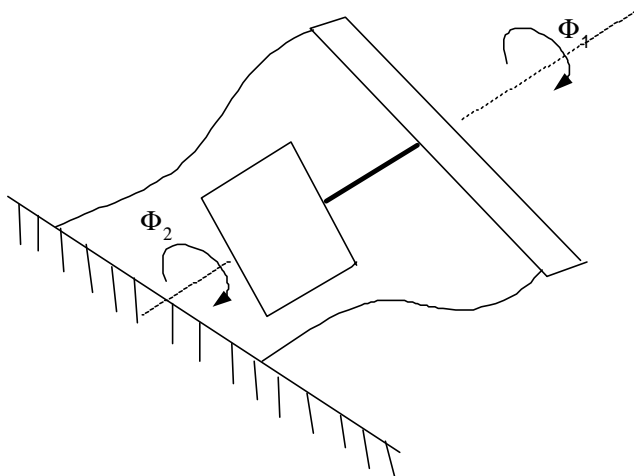


Fig. 12.

Free body diagrams followed by application of Newton's Law results in the following system equation,

$$\left[I_1' I_2' s^4 + (I_1' b_4 + I_2' b_3) s^3 + \{ I_1' K_2 + I_2' (K_1 + K_2) + b_3 b_4 \} s^2 \dots \dots \dots \{ K_2 (b_3 + b_4) + K_1 b_4 \} s + K_1 K_2 \right] \Phi_2 = K_2 c_2 V_{in} \quad (8)$$

Using the characteristic polynomial of the system we can easily calculate the torsional mode frequencies and the corresponding quality factors. Numerical results based on the above analysis are presented in the next section.

5. Numerical Results obtained using MATLAB

We can now use the preliminary dimension values obtained in Section 3 and equations derived in Section 4 to obtain numerical results in MATLAB. The relevant MATLAB code is included in the Appendix A. After multiple iterations, a set of dimensions are chosen to provide the most optimal performance of the scanning mirror. These iterations are based on fabrication constraints, separation and isolation of the operating natural frequencies, maximization of decoupling of the two scanning modes, and minimization of translation errors. The optimum system dimensions are provided in Appendix A.

Using these values, bode plots for the bending and torsion dynamics were obtained in MATLAB (Fig. 13).

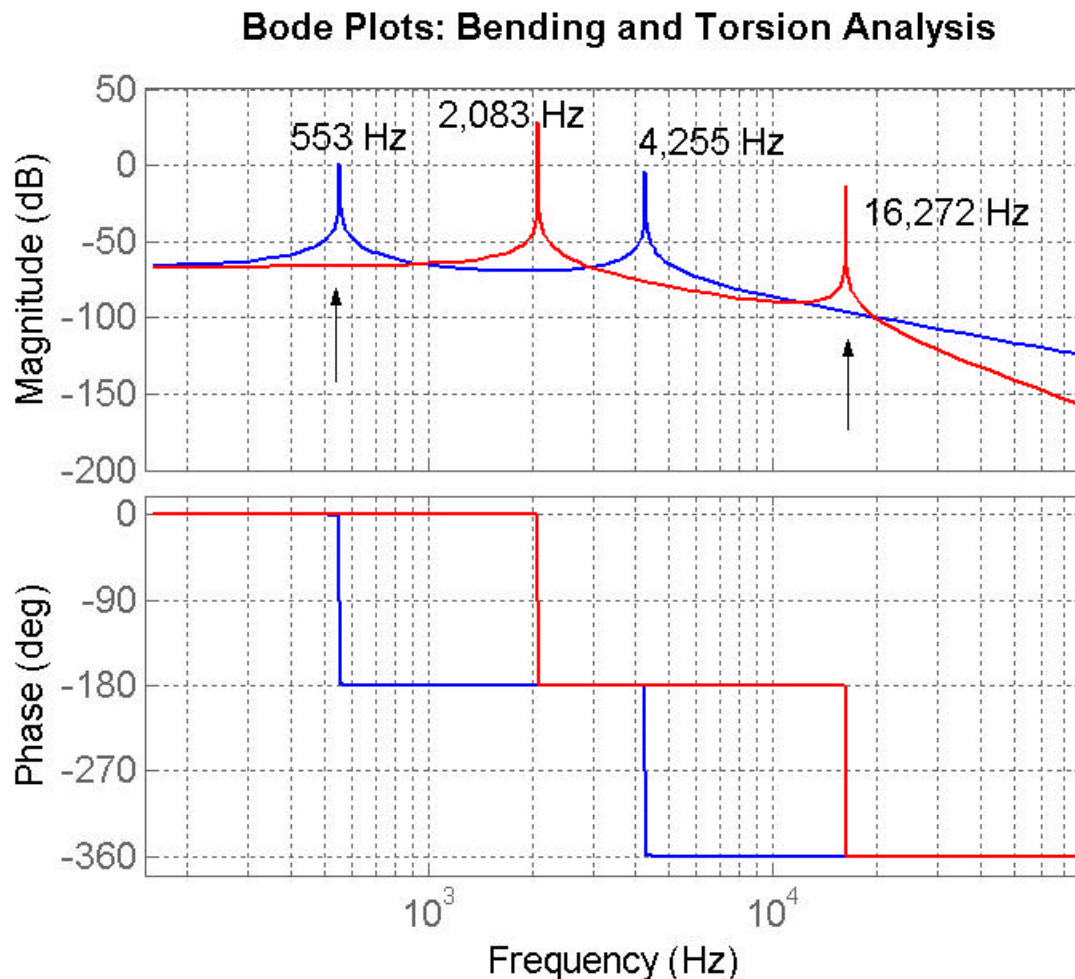


Fig. 13 Frequency response plots for the models derived in Section 4

Bending Analysis (Blue Graph)

Mode 1: $\omega_1=553$ Hz, $Q_1=1740$

Mode 2: $\omega_2=4225$ Hz, $Q_2=2700$

Torsional Analysis (Red Graph)

Mode 1: $\omega_3=2083$ Hz, $Q_3=56000$

Mode 2: $\omega_4=16.3$ kHz, $Q_4=26190$

The quality factors mentioned here result from the damping coefficients derived in Section 7. These quality factors are very high which is typical of a resonant system. The range of motion of the mirror in close to resonance operation is critically dependent on these quality factors and the geometry of the PZT actuators deposited at the cantilevers' bases. Using the Q-factor values mentioned above and the PZT model discussed in Section 8, we were able to predict a sensitivity of $5.7^\circ /V$ for the bending mode and $1.8^\circ /V$ for the torsion mode. As is mostly the case, the model for damping provides only an order of magnitude estimate for the actual dissipation present in the system. Better characterization of damping can be done by experimental measurements, which would yield more accurate values for the quality factors.

So as to operate in the linear region (with respect to time) of the scan, we try to aim for scan angles of $\pm 10^\circ$ (mechanical). The above analysis shows that this desired range of motion can be easily achieved with voltages less than 20V, but an exact value of sensitivity will be obtained only after experimental measurements. Also the current consumption can be estimated by equating the electrical power input to the system with the power dissipated due to damping. For 20 V input voltage, this results in a current consumption of far less than 1mA.

6. Finite Element Analysis

In the previous section we used the device dimensions to predict the system response using an analytical model, with the help of MATLAB. In this section, we perform the same analysis using Finite Element Techniques, and then compare the results of the two analyses. We use Pro/E and Pro/Mechanica to run a finite element based modal analysis on our device geometry. The results of this modal analysis are presented in figures 14 and 15, and in Table 1.

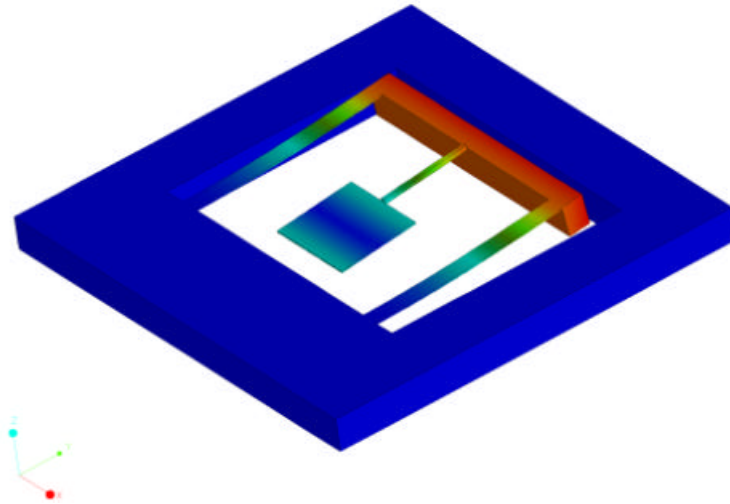


Fig. 14. FEM Results: First Bending Mode (562 Hz)

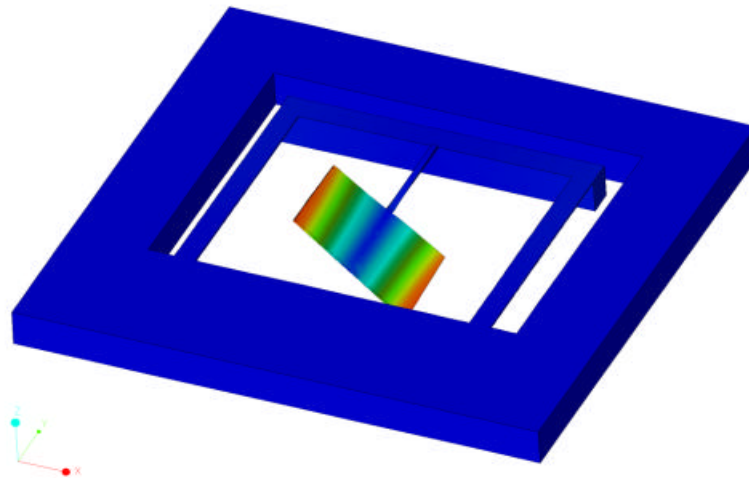


Fig. 15 FEM Results: Second Torsion Mode (15.54 kHz)

| Vibration Mode | Description | FEM Results | Analysis & MATLAB Results |
|----------------|---|------------------|---------------------------|
| 1 | Simple Bending of the Cantilevers | 562 Hz | 553 Hz |
| 2 | Simple Torsion of the Cantilevers | 2190 Hz | 2083 Hz |
| 3 | Compound Bending of the Cantilever (2 nd bending mode) | 3025 Hz | 4225 Hz |
| 4 | In-plane Bending of the Torsion Bar | 5623 Hz | |
| 5 | In plane bending of cantilever beams and torsion bar | 11.67 kHz | |
| 6 | Out-of-plane Bending of the Torsion Bar | 12.63 kHz | |
| 7 | Pure Torsion of the Torsion Bar | 15.54 kHz | 16.27 kHz |

Table 1. Comparison of the FEM and MATLAB results

The bending analysis predicts only Modes 1 and 3 of the system, while the torsion analysis predicts Models 2 and 7 of the system. The results of FEM modal analysis and lumped parameter modeling followed by MATLAB agree well. The most noticeable difference is in Mode 3. The reason for this discrepancy is that the bending analysis assumes the torsion bar to be infinitely stiff in bending. In the third mode, the compliance of this torsion bar starts manifesting itself. Hence the actual stiffness in the system is somewhat less than what the model accounts for. Therefore, the FEM predicted value for the natural frequency of the third mode is relatively lower. It is noteworthy that the two operating modes, 1 and 7, are spaced widely apart and are also not dangerously close to any other modes.

We also performed a dynamic boundary condition analysis in Pro/Mechanica to verify if the two mode that we are interested in could be exclusively excited by an actuation only at the base of the two cantilevers. The results confirmed our hypothesis, and consequently in the fabrication process PZT actuators were deposited only at the cantilever base. Furthermore, for the quality factors obtained in the previous section, this dynamic boundary condition analysis gave us a sensitivity value of 15°/V. This is of the same order of magnitude as the analytical results of Section 6.

7. Damping Analysis

As mentioned earlier, an estimate of the dissipation in the system is necessary to predict the electrical power required to generate the desired amount of mirror deflection. Air damping and hysteresis are the two modes of dissipation present in the scanner structure. In this section we present a model of viscous damping due to the motion of the structure in air. Detailed device geometry is presented in Section 10 which discusses the device fabrication. Figure 31 illustrates that the mirror vibrates in free air without any substrate beneath. This eliminates any squeeze film damping.

Damping of the intermediate mass translation during beam bending: b_1

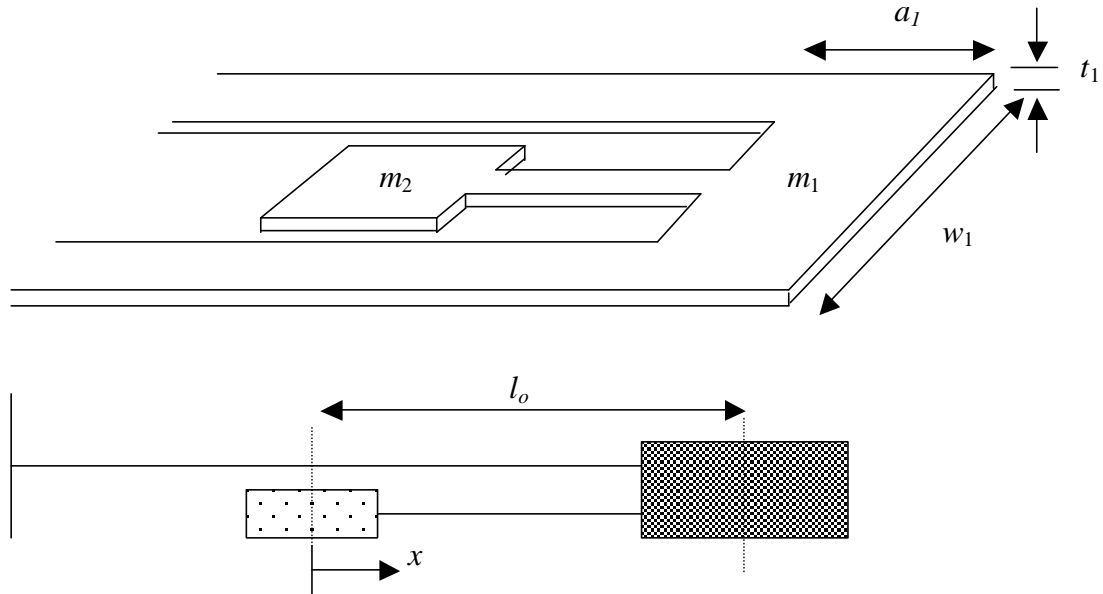


Fig. 16. Sketch of scanner structure

For very small body sizes, the Reynold's number (R) is typically low. For low Reynold's number flows ($R \sim 1$), Stokes' approximation holds [11]. To determine whether Stokes' Law can be applied to our analysis, we calculate the Reynolds number as follows.

The mirror deflection resulting from the cantilever bending is given by

$$\mathbf{q}_1 = \mathbf{q}_{\max} \sin(2\mathbf{p}f)t \quad (9)$$

where \mathbf{q}_{\max} is the amplitude of the mirror deflection, and f is the scan frequency, 562 Hz in this case. Then the angular velocity of the mirror and intermediate mass is

$$\dot{\mathbf{q}}_1 = (2\mathbf{p}f)\mathbf{q}_{\max} \cos(2\mathbf{p}f)t = \mathbf{w}\mathbf{q}_{\max} \cos \mathbf{w}t \quad (10)$$

If the center of the intermediate mass is located at distance of l_o from the virtual pivot of rotation (Fig. 16), then its velocity, V_{\max} is simply:

$$V_{\max} = l_o \dot{\mathbf{q}}_{\max} = l_o \mathbf{q}_{\max} \boldsymbol{\omega} \quad (11)$$

For $l_o = 1.573$ mm, a maximum scan angle of 10° , or 0.17 rad, and a scan frequency of 562 Hz, the maximum translational velocity of the intermediate mass m_1 is obtained to be 0.944 m/s. The Reynolds number is given by:

$$R = \frac{V_{\max} t_1}{\boldsymbol{\nu}_0} \quad (12)$$

where $\boldsymbol{\nu}_0$ is the kinematic viscosity of air, which has a value of 1.51×10^{-5} m²/s. For a thickness of $t_1 = 370$ μm , this gives a Reynolds number of **23.1**.

As we can clearly see from the above estimates, the Reynolds number for our system is much greater than 1. Analysis in the intermediate Reynolds number range ($10 < R < 10^3$) is extremely difficult to carry out [19]. Therefore, in order to keep our model simple, we base our estimate on Stokes' Law even for a relatively high Reynold's number. However, we recognize the fact that this simplifying assumption will result in an underestimation of the actual damping that is present in the system. Hence, in order to compensate for this underestimation, as well as to take into account the material damping that is inherent in the system which is otherwise unmodelled, we multiply the damping estimate based on Stoke's approximation by an empirical factor of 10. This allows us to conservatively size the actuators.

Based on Stokes' Law is valid, the viscous force, F , acting on mass m_1 in translation is given by:

$$F = C_D \boldsymbol{h} w_1 V \triangleq b_1 V \quad (13)$$

where C_D is the viscous drag coefficient and \boldsymbol{h} is the dynamic viscosity of air. An approximate value for the drag coefficient, $C_D = 8$, is obtained from a table of drag coefficients for standard geometries [11]. For air at room temperature and pressure, $\boldsymbol{h} = 2 \times 10^{-5}$ Ns/m². Therefore, for $w_1 = 3$ mm, we have $\boldsymbol{b}_1 = 4.8 \cdot 10^{-7}$ Ns/m. As explained above, we will assume $\boldsymbol{b}_1 = 4.8 \cdot 10^{-6}$ Ns/m.

Damping of the mirror and intermediate mass rotation due to beam bending: b_2

In this analysis, we estimate the drag moment generated on the rotating mirror and intermediate mass, computed about the CG, using the result obtained in the previous section. We make this estimate by considering the effects of the two masses separately.

For the first mass m_1 , we make the simplifying assumption that the drag force acting on mass m_1 as it rotates about the virtual pivot P, is approximately constant, given by Equation (13). The schematic is as shown below:

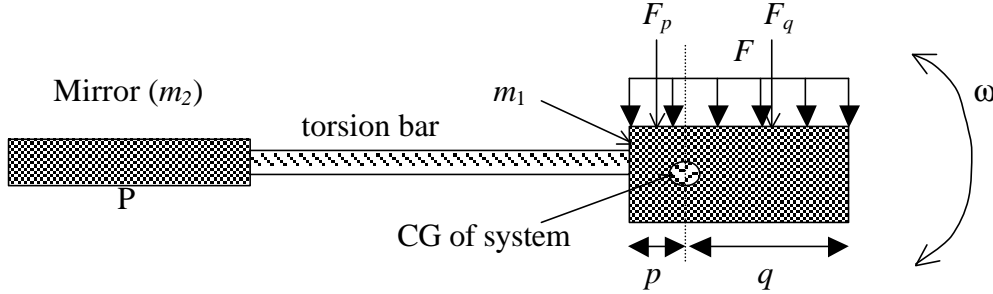


Fig. 17. Rotation of mass m_1

F_p and F_q are the effective drag forces acting on mass m_1 computed on either side of the system CG,

$$F_p = \frac{Fp}{p+q} \quad ; \quad F_q = \frac{Fq}{p+q} \quad ; \quad F_p + F_q = F \quad (14)$$

Therefore, the moment, M_1 , on the structure about its CG, due to the viscous forces on mass m_1 , is simply,

$$M_1 = F_q \frac{q}{2} - F_p \frac{p}{2} = \frac{F}{2}(q-p) \quad (15)$$

$$\Rightarrow M_1 = \frac{b_1 l_o \mathbf{q}_{\max}(q-p)}{2} \mathbf{w} \quad (16)$$

Next, we find the moment, M_2 , about the structure CG due to the viscous forces acting on mass m_2 (the mirror) as it rotates about point P .

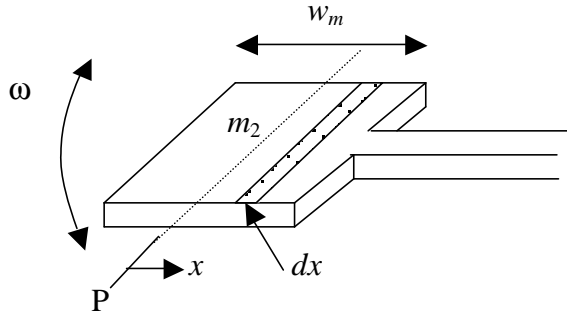


Fig. 18. Rotation of mass m_2

From Equation (13), we know that $F = b_1V$. Therefore, the pressure, p , on mass m_2 is given by:

$$p = \frac{F}{w_m^2} = \frac{b_1V}{w_m^2} \quad (17)$$

Taking a differential element, dx , on m_2 , the differential force, dF , is:

$$dF = pw_m dx = \frac{b_1V}{w_m} dx \quad (18)$$

Using Equation (11), the maximum velocity, V_{\max} , at any position x along w_m then becomes:

$$V_{\max} = x\mathbf{q}_{\max}\mathbf{w} \quad (19)$$

Substituting Equation (19) into Equation (18), we now have:

$$dF = \frac{b_1\mathbf{q}_{\max}\mathbf{w}}{w_m} x dx \quad (20)$$

The differential moment, dM_2 , at a certain distance x about P , the virtual center of rotation, then becomes:

$$dM_2 = \frac{b_1\mathbf{q}_{\max}\mathbf{w}}{w_m} x^2 dx \quad (21)$$

Therefore, the moment, M_2 , of the entire mass m_2 about P is:

$$M_2 = 2 \int_0^{\frac{w_m}{2}} \frac{b_1\mathbf{q}_{\max}\mathbf{w}}{w_m} x^2 dx = \frac{1}{12} b_1\mathbf{q}_{\max} w_m^2 \mathbf{w} \quad (22)$$

Since this is a pure moment, moment computed about point P is the same as the moment about the CG, or any other point on the structure. Finally combining M_1 and M_2 , the damping moment, M , generated on the structure about its CG, as it rotates about the virtual pivot P during cantilever bending, can be expressed as,

$$M = M_1 + M_2 = \left[\frac{b_1 \mathbf{q}_{\max}}{12} (6l_o (q-p) + w_m^2) \right] \mathbf{w} = b_2 \mathbf{w} \quad (23)$$

$$\Rightarrow b_2 = \frac{b_1 \mathbf{q}_{\max}}{12} (6l_o (q-p) + w_m^2) \quad (24)$$

We have found that $b_1 = 4.8 \times 10^{-6}$ Ns/m. Further, we know that $l_o = 1.573$ mm, $\mathbf{q}_{\max} = 10^\circ = 0.17$ rad, $w_m = 0.9$ mm, $p = 9$ μm , and $q = 211.1$ μm . These give us a value of 1.68×10^{-13} Nsm for b_2 . Multiplying this by the previously explained factor of 10, we have $b_2 = 1.68 \times 10^{-12}$ Nsm.

Damping of the mirror and intermediate mass rotation due to twisting of the torsion bar: b_3 and b_4

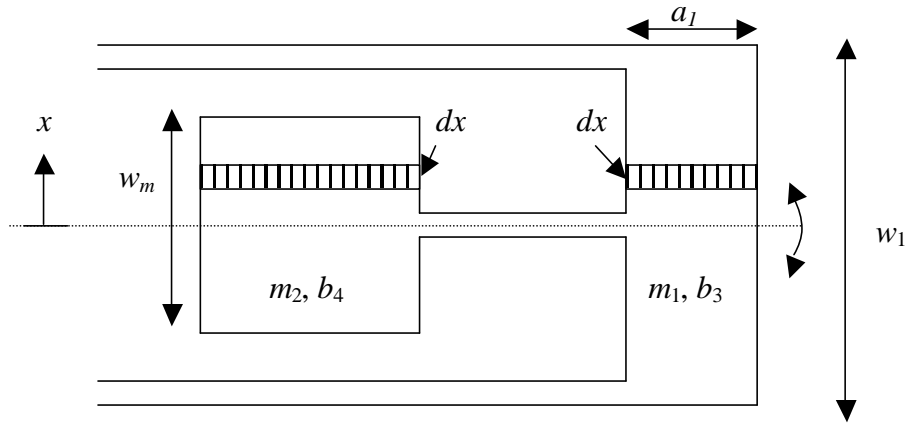


Fig. 19. Top view of scanning system

We first consider the intermediate mass m_1 . From Equation (13), we know that $F = C_D \mathbf{h} w_1 V$. Therefore, average pressure, p , on the intermediate mass surface is:

$$P = \frac{C_D \mathbf{h} w_1 V}{w_1 b} = \frac{C_D \mathbf{h} V}{b} \quad (25)$$

Using a similar argument as before, we find that the differential force and moment at a certain distance x , dF and dM respectively, are given by:

$$dF = C_D \mathbf{h} \mathbf{q}_{\max} \mathbf{w} x dx \quad (26)$$

$$\Rightarrow dM = C_D \mathbf{h} \mathbf{q}_{\max} \mathbf{w} x^2 dx \quad (27)$$

Therefore, the moment of the entire mass m_1 about the centerline is:

$$M = 2 \int_0^{w_1} C_D \mathbf{h} \mathbf{q}_{\max} \mathbf{w} x^2 dx = \frac{1}{12} C_D \mathbf{h} \mathbf{q}_{\max} w_1^3 \mathbf{w} = b_3 \mathbf{w} \quad (28)$$

This gives us an equation for b_3 :

$$b_3 = \frac{1}{12} C_D \mathbf{h} \mathbf{q}_{\max} w_1^3 \quad (29)$$

Substituting the appropriate values, we find that $b_3 = 6.12 \cdot 10^{-14}$ Nsm. Therefore, we take $b_3 = 6.12 \cdot 10^{-13}$ Nsm.

Using exactly the same argument, we can easily prove that:

$$b_4 = \frac{1}{12} C_D \mathbf{h} \mathbf{q}_{\max} w_m^3 \quad (30)$$

For $w_m = 0.9$ mm, we have $b_4 = 1.65 \cdot 10^{-15}$ Nsm. Therefore, we take $b_4 = 1.65 \cdot 10^{-14}$ Nsm.

8. Actuation

Comparison of Actuation Schemes

Several actuation methods were considered in designing our scanning mirror. Possible options included: electromagnetic, electrostatic, piezoelectric and thermal actuation. After some deliberation, however, the piezoelectric configuration was decided upon because of the following reasons:

- *Electromagnetic actuation*, although provides relatively large forces and has high repeatability, is poor in high-frequency operations [20]. External coils that are needed to produce the magnetic field required for actuation might also present a problem in fabrication and packaging [21].
- *Electrostatic actuation* is versatile and simple [22]. However, it is well known that there is an electrostatic instability associated with such an actuation (i.e. the pull-in voltage). In addition, a major disadvantage of electrostatic actuation lies in its non-linearity [23]. The crosstalk is too large to achieve an independent control of the angles, which is a critical component in the design of our scanning device. This problem has been addressed by Toshiyoshi *et al.* Furthermore, the voltage required to actuate a device with a size like ours is in the order of hundreds of volts [14]. For these reasons we decided to bypass this option and look for a better alternative.
- *Thermal actuators* have inherent limitations for long-term use because, at high temperatures, silicon can lose the nearly perfect linear-elastic properties that makes the material so attractive for MEMS [24]. Another major disadvantage of thermal actuators is their large power consumption [24].
- *Piezoelectric actuators* were finally chosen because of their rapid response [22] to the alternating voltage input required to drive the MEMS structure at its higher resonant frequency of 15.5 kHz. They are also highly repeatable and very reliable for MEMS applications [20].

Details of Piezoelectric Actuation

Piezoelectric actuation was selected for the OCT scanning device due to the ability to achieve high strains at high frequencies. A piezoelectric is actuated by taking advantage of coupling between the mechanical and electrical properties of the material. Application of a voltage across the material will cause an expansion or constriction in the piezo film. A thin piezo film will be applied on bending silicon beams to excite desired deflection modes dependent on natural frequencies. An exaggeration of static deflection in the beams is shown below in Fig. 20. As the piezo contracts along its length, traction between the piezo and silicon beam causes the structure to deflect. This static deflection is used only to excite the beam and is a lower value than the total deflection achievable at the beam's natural frequency.

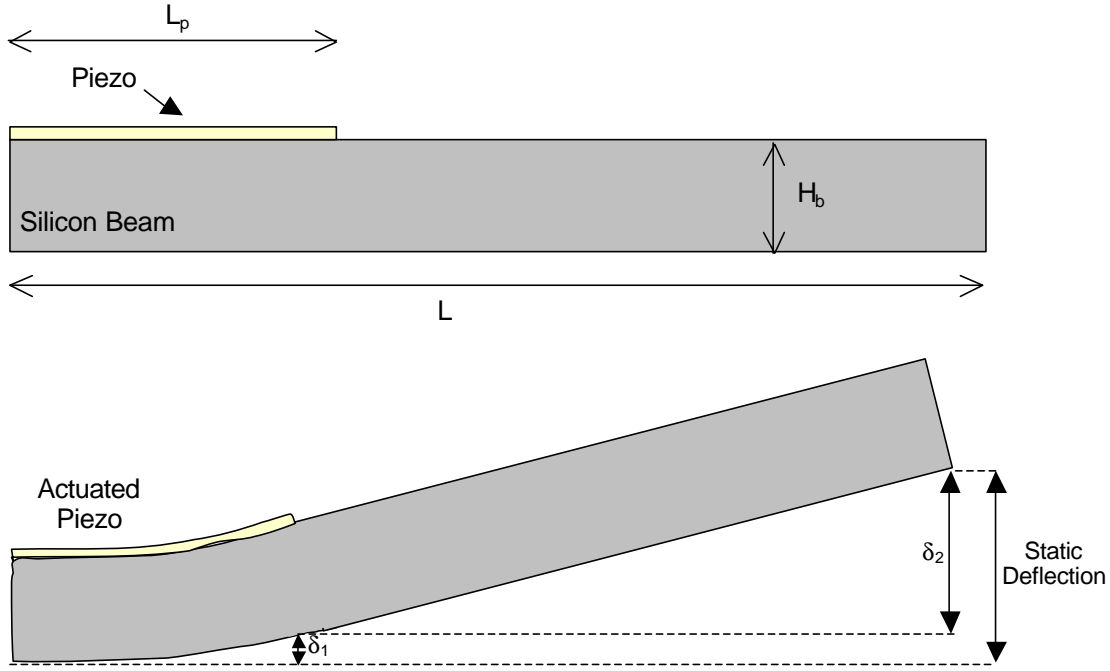


Figure 20. Top: PZT piezoelectric patterned onto a partial length of a silicon beam. Bottom: Constriction of the piezo along its length results in the silicon beam deflection upward

Bending of the beam in the piezo region is dependent upon the moment applied by the film. This moment, M , is described in equation (31).

$$M = \frac{6I_b V_{in}}{H_b^2} \begin{pmatrix} c_{13} e_{33} & -e_{31} \\ c_{33} & \end{pmatrix} \quad (31)$$

The moment is dependent upon the silicon beam's moment of inertia, I_b , as well as the height of the beam H_b . It is also linearly dependent on the voltage applied through the piezo material. The "c" terms are from the stiffness matrix for the piezo material and the "e" terms are derived from the piezoelectric constants of the material. Full derivation of these values using data from literature can be found in Appendix B. These values can vary significantly depending on the process used for fabricating the film as well as the resulting film structure.

Deflection of the silicon beam at the end of the piezo region can be found with respect to the applied moment in equation (31). This deflection, shown in equation (32), is once again linearly related to the voltage, V_{in} .

$$d_1 = \frac{Ml^2}{2\tilde{E}I_b} = \frac{3V_{in}l^2}{\tilde{E}H^2} \begin{pmatrix} c_{13} e_{33} & -e_{31} \\ c_{33} & \end{pmatrix} \quad (32)$$

This deflection term is inversely related to the height of the beam squared, as well as the biaxial modulus, \tilde{E} . The length, L_p , is that of the piezo material along the beam. The deflection value

only represents the piezo region, but using the angle of the beam at the end of the piezo region, the deflection of the non-piezo region can also be calculated. Equation (33) describes this angle and the subsequent total deflection is given in equation (34).

$$\mathbf{q}_o = \frac{6VL}{\tilde{E}H^2} \left(\frac{c_{13}e_{33}}{c_{33}} - e_{31} \right) \quad (33)$$

$$x_o = \mathbf{d}_1 + (L-l)\sin\mathbf{q}_o \quad (34)$$

The term, L_p , is the length of the piezo covered region, and L is the length of the entire beam. In order to eliminate the need for calibration, a linear relationship between the voltage and deflection is desirable. The total deflection is linearly related to the voltage in the δ_1 term, but has a sine dependence on voltage from the θ_o term. Because deflection angles will be limited to a range of $\pm 10^\circ$, the small angle approximation for sine is applicable. To verify this, the deflection was plotted vs. voltage, shown in Figure 21, using anticipated dimensions, material properties, and voltages between 1 and 20 V.

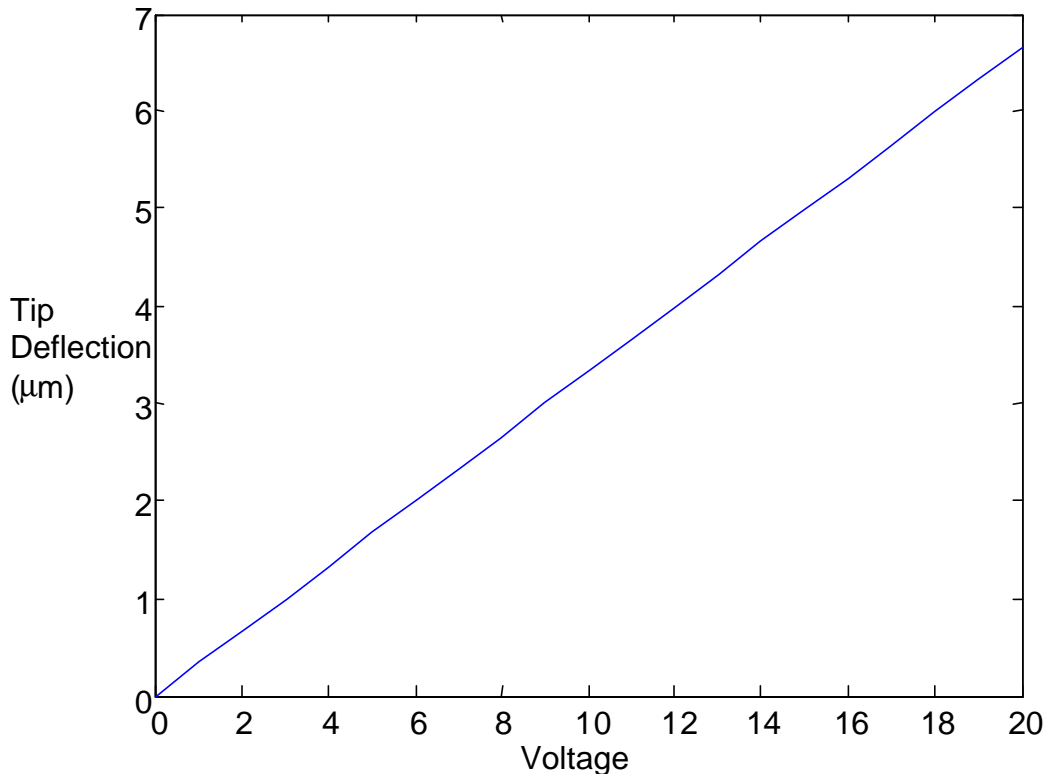


Figure 21: Tip deflection vs. voltage in the anticipated range

As expected, the tip deflection has a predominantly linear relationship with voltage in the range of operating voltages for the device. A static deflection of up to 7 µm is achievable with only 20 V applied across the piezo film.

9. Analysis of Other Modeling Issues

Deflection due to Gravity

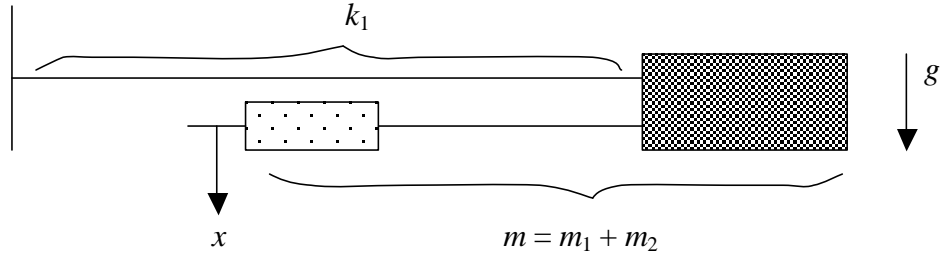


Figure 22. Sketch of structure under the action of gravity

The static deflection, x , of the mirror due to the action of gravity (in the worst case scenario where the mirror is completely horizontal, and therefore perpendicular to the direction of action of gravity) is found by resolving forces in the vertical direction:

$$k_1 x = mg \quad (35)$$

From MATLAB, we found that $k_1 = 36.5 \text{ N/m}$, and $m = 68 \text{ mg}$. Taking $g = 9.81 \text{ m/s}^2$, the static deflection of the mirror is therefore found to be only $0.183 \text{ } \mu\text{m}$. Given that this is less than $1 \text{ } \mu\text{m}$ and is just 0.9% of the thickness of the mirror, we ignore the static deflection of the mirror due to the action of gravity.

Dynamic Deformation of the Mirror [25]

The Rayleigh Limit – the maximum amount of surface deformation tolerable without significant degradation in image quality – allows a peak-to-valley surface deformation, d , of $\frac{l}{4}$. Here, l refers to the wavelength of the incident light, which, for our scanning device, is 850 nm . Therefore, we need $d < 212.5 \text{ nm}$.

The nonplanar surface deformation, d , (shown in Fig. 23 below) is given by

$$d = 0.183 \frac{r(1-n^2)(2pf)^2 q}{Et^2} \left(\frac{l}{2}\right)^5 \quad (36)$$

where: $r = \text{material density} = 2,330 \text{ kg/m}^3$

n = Poisson's ratio = 0.278
 f = higher scan frequency = 15.5 kHz
 q = mechanical half-angle mirror scan = $10^\circ = 0.17$ rad
 E = Young's modulus = 130 GPa
 t = mirror thickness = 20 μm
 l = mirror length = 0.9 mm

Therefore, the nonplanar surface deformation of our mirror at the higher scan frequency of 15.5 kHz is **212.1 nm**. This value is approximately equal to the Rayleigh Limit of 212.5 nm for our mirror, hence showing that nonplanar surface deformation is not a problem.



Fig. 23. Nonplanar surface deformation of mirror

Fatigue from Bending

Stress concentration factors have not been included in the following analysis because we intend to use generous fillet radii in the structure design.

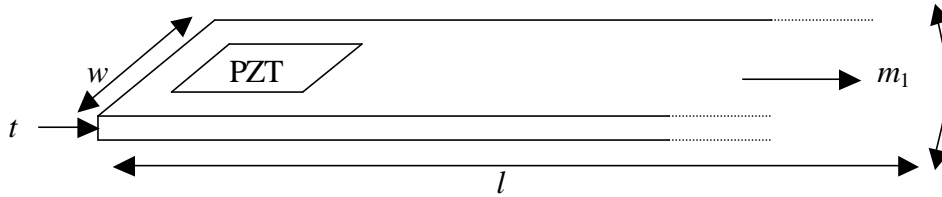


Fig. 24. Sketch of bending beam

Given that each of the two bending beams supporting mass m_1 (one of which is shown above) deflect by a maximum angle, q_{\max} of 10° , or 0.17 rad, we can find the force, F , associated with this deflection using the following equation:

$$F = \frac{2EIq_{\max}}{l^2} = \frac{Eq_{\max}wt^3}{6l^2} \quad (37)$$

The moment, M , due to the force F is thus:

$$M = Fl = \frac{Eq_{\max}wt^3}{6l} \quad (38)$$

For $l = 2.25$ mm, $E = 130$ GPa, $w = 200$ μm and $t = 20$ μm , we find that the moment experienced by each beam is 2.62×10^{-6} Nm. Using a factor of safety of 2, we let the moment be 5.24×10^{-6} Nm. Therefore, the maximum bending stress, s_{\max} experienced by each of these bending beams is:

$$s_{\max} = \frac{Mc}{I} = \frac{M}{24wt^2} \quad (39)$$

which gives us a maximum bending stress of **2.73 MPa** for each beam. This is significantly below the yield strength of silicon (2,800 – 6,800 MPa [26]). Therefore, we can safely conclude that fatigue by cyclical bending of the beams is not a concern.

Fatigue from Torsion

In analyzing the torsion on the torsion bar holding the mirror, we first note that the polar moment of inertia, I_p , of the square cross-section of the bar is:

$$I_p = \frac{w_2^4}{6} \quad (40)$$

where w_2 is the width and thickness of the square rod, and has a value of 50 μm . Therefore, we find that $I_p = 1.04 \times 10^{-18}$ m⁴.

The angle of rotation, q , is related to the torsion, T , by the following equation:

$$q = \frac{Tl_2}{GI_p} \quad (41)$$

where l_2 is the length of the torsion bar, which is 1 mm, and G is the shear modulus of the bar, which we found from MATLAB in our analysis to be 50.8 GPa. Hence, using Equation (41), we find that the maximum torsion on the bar, corresponding to the maximum scan angle of 10°, or 0.17 rad, is 8.98×10^{-6} Nm. Again, using a factor of safety of 2, we let the torsion be 1.8×10^{-5} Nm.

We can now calculate the maximum shear stress, t_{\max} on the torsion bar using the following equation:

$$t_{\max} = \frac{Tr_{\max}}{I_p} \quad (42)$$

where r_{\max} is the radial location of the furthest point on the section from the axis. In this case, r_{\max} would be equal to $w_2/\sqrt{2}$. Therefore, $t_{\max} = \mathbf{611\ MPa}$. Again, we find that this is significantly below the yield strength of silicon (2,800 – 6,800 MPa [26]). Hence, we can also safely conclude that fatigue by cyclical torsion of the bar holding the mirror is not a concern either.

In reality, brittle materials, like silicon, are normally not expected to suffer from cyclic fatigue because they are hard and have relatively little plasticity. This is especially so for single crystal silicon. Fatigue failure occurs as a result of crack propagation. Cracks primarily arise from imperfect crystal structures and grain boundaries. Since single crystal silicon has very low crystal defects (dislocations, vacant sites, grain boundaries, etc.), the chances for crack development and propagation are low and hence fatigue failure is typically not a critical problem [27].

Instead, according to Muhlstein *et al* [28], fatigue of silicon is most likely due to environmentally assisted hydration cracking rather than cyclic plasticity. Experimental evidence revealed that silicon does not display the room temperature plasticity or extrinsic toughening mechanisms necessary to cause fatigue in either ductile (e.g. metals) or brittle (e.g. ceramics and ordered intermetallics) materials. Instead, the authors found that fatigue of silicon in MEMS applications occurs through a process of sequential, mechanically induced oxidation and environmentally assisted cracking of the surface layer of the material that forms upon reaction with the atmosphere (e.g. the SiO₂ “native oxide”) that they termed *reaction-layer fatigue*. This phenomenon is also referred to as *corrosion fatigue* in the technical literature. Further investigation needs to be carried out to obtain more definitive data in this area.

10. Fabrication

Fabrication of the scanning device begins with an SOI wafer as in figure 25. The handle wafer thickness is 350 μm separated by 0.5 μm of silicon dioxide from the 40 μm top layer of silicon. SOI wafers at these specification are available directly from suppliers and therefore require no additional processing [21].

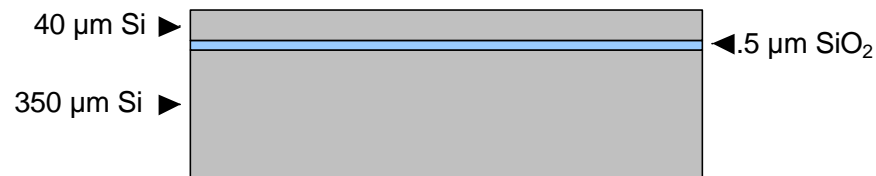


Figure 25. SOI wafer with a thick secondary layer of silicon

The final thickness of the scanning mirror and supporting structures will be 20 μm except for a small area that will be 40 μm . This larger thickness determined the thickness of the secondary silicon on the SOI wafer. The handle wafer thickness of 350 μm is the minimum requirement for an SOI wafer with a 40 μm secondary layer.

The buried silicon dioxide is advantageous in this process because it provides an etch stop when using DRIE. The backside of the wafer is etched up to this oxide layer to create open space below the mirror.

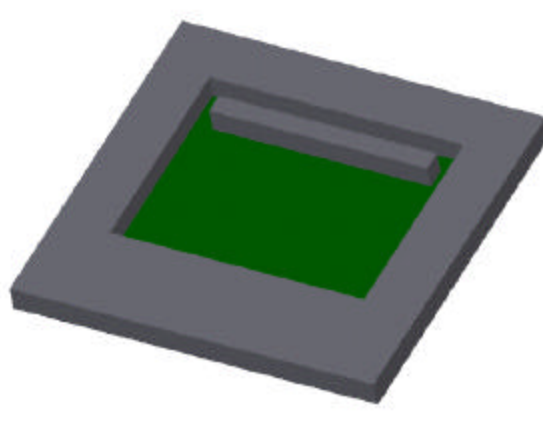


Figure 26. Backside DRIE etch to create open area beneath mirror and pattern the mass feature.

A large mass with a full wafer thickness is necessary for optimal dynamic response and is patterned during this DRIE etch as shown in figure 26. The remaining oxide layer is not removed as it will be necessary later in a later process.

The next step in the process is a large area DRIE etch on the front side of the wafer to create a torsional stiffening feature. An area slightly larger than the final device dimensions is etched 20 μm , leaving 20 μm of silicon protruding from the surface as shown in figure 27.



Figure 27. Front side etch to produce a stiffening feature for the torsional beam

One concern with creating this raised feature is that subsequent photolithography on the depressed region will suffer from some image distortion due to proximity exposure. The distance between a mask and photoresist on the surface would be a minimum of 20 μm . Equation (43) (Klint, can you please include the references that Xueen provided) describes the resolution limit, b , based on the wavelength, λ , of the UV light source and the proximity between the mask and photoresist, s .

$$b = 3/2 \sqrt{\frac{\lambda s}{2}} \quad (43)$$

The resolution for a 365 nm UV light source and a conservative separation distance of 30 μm is approximately 5 μm . Since the smallest feature size for the scanner is 75 μm wide, the distortion caused by the protrusion is not an issue.

The next step in the process is to deposit a 250 nm silicon dioxide layer to insulate electrodes for the PZT from the silicon substrate. The oxide layer is deposited using CVD then etched in an RIE. With the insulating layer down, a layer of photoresist for a lift-off process is spun on and patterned, leaving open areas on the oxide for electrodes. A 100 \AA adhesion layer of titanium is evaporated onto the oxide followed by 1000 \AA of platinum. After stripping the resist, four electrodes remain which will act as the ground for voltages across the PZT.

The PZT piezoelectric material is then spun onto the substrate in sol-gel form. An example of the solution used for this process and the processing steps are included in figure 28. Only thin layers of PZT can be formed during each iteration due to condensation and annealing requirements of the material. The process produces a 150 nm film per iteration.

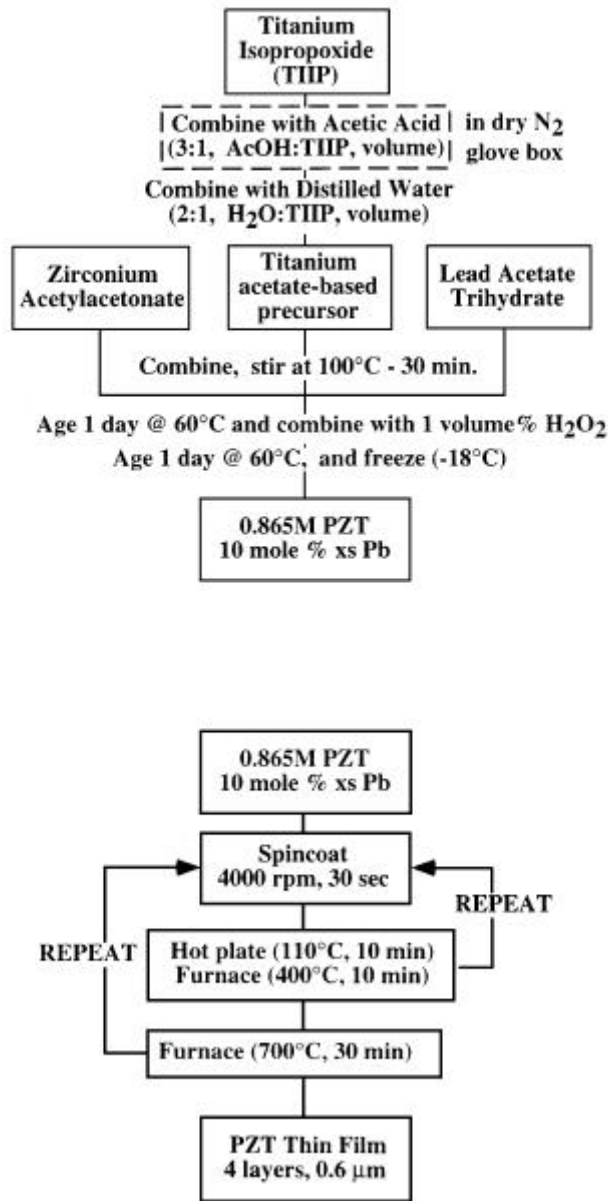


Figure 28. Sol-gel Processing for PZT [30]

The structure of the PZT film is very sensitive to the annealing process as well as the electrode material beneath it. Platinum is the most commonly used electrode material due to its [111] texture [30]. Annealing the PZT film requires a two-step process to produce the [100] texture desired for the optical scanner. If the PZT were rapidly heated to 600 °C, a [111] texture would develop [31].

Once deposited, the PZT must be masked and patterned. Photoresist is used as the masking layer for the wet-etch technique used. In the first of two steps from the etching process developed by Wang et al., PZT can be etched at 0.13 (m/min using 10:1 buffered oxide etch (10 HN4F:1HF) [32]. This etch leaves a whitish residue on the etched area which is removed in the second

etching step with 2HCl:H₂O at an elevated temperature of 45 °C for 30 seconds. The use of buffered HF in the first step of this process was the reason for leaving the oxide on the backside of the wafer. This helps reduce potential undercutting during the PZT etch. The four etched PZT pads to be used for actuation are shown in figure 29.

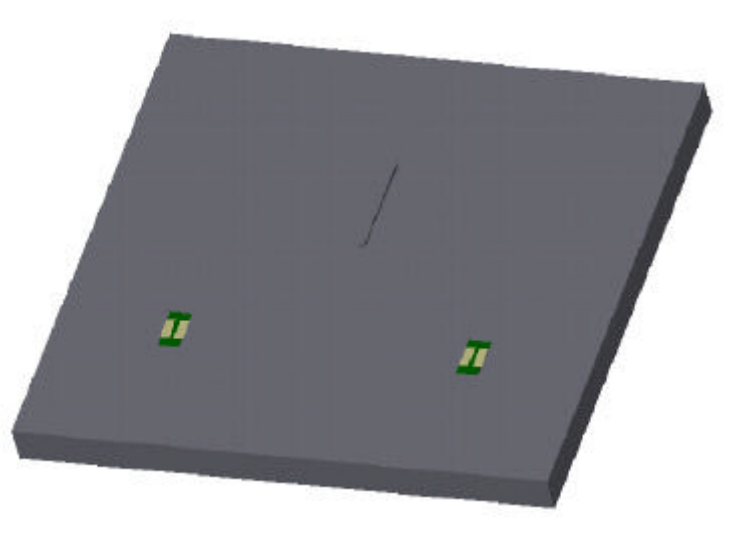


Figure 29. Oxide insulation with electrodes and patterned PZT

Before patterning the top electrodes for the PZT, another insulating layer of oxide is necessary to avoid shorting between the top and bottom electrodes. This .25 μ m oxide layer is once again deposited using CVD and etched in an RIE. As in the lift-off process for the bottom electrodes, a 100 Å adhesion layer of titanium is evaporated onto the oxide followed by 1000 Å of platinum. The mask for the top electrodes also contains traces to a 350 μ m by 350 μ m contact pad for wire bonding to the external electronics. These features are shown in figure 30.

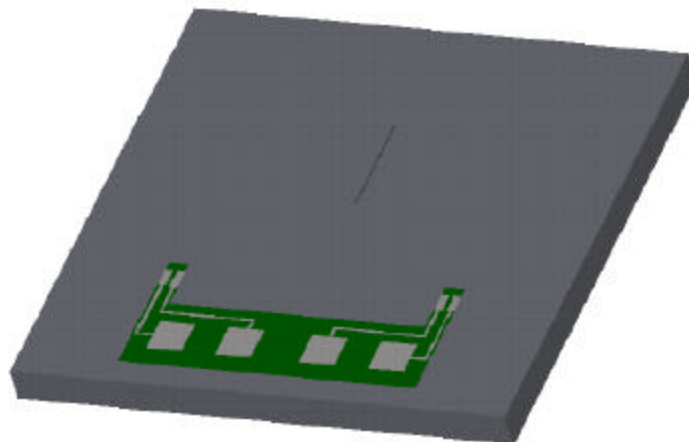


Figure 30. Top electrodes pattern including leads and contact pads

To provide a more reflective surface on the scanner mirror, evaporated aluminum is patterned onto the area using a lift-off process with a chrome adhesion layer. The mirror surface is the last deposition necessary in the process.

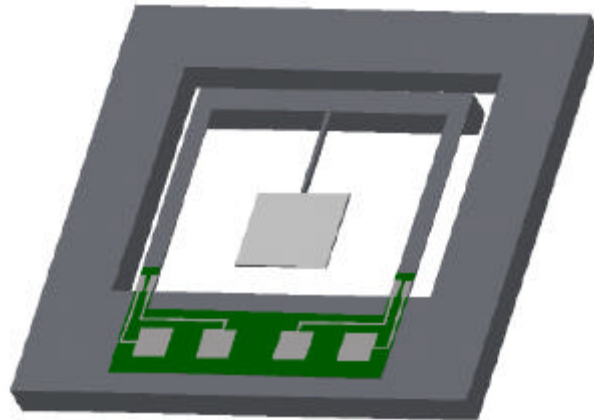


Figure 31. Final DRIE etch releases mirror and beams

The final step is a DRIE etch to define the features of the mirror and supports. DRIE is used instead of KOH due to the insulating oxide layers on the surface of the device. Photoresist is used as the masking layer for this relatively short 20 μm etch. The final device, as it would look after dicing, is shown in figure 31.

Before using the PZT actuators, they must be poled in order to yield the highest amount of strain for the voltages applied. As shown in figure 32, an large initial electric field is needed in order to reach the saturation point for the net polarization [30]. This net polarization affects the piezoelectric coupling constant and therefore the strain achievable from the material. If this initial poling is not performed, the PZT will operate along a much smaller hysteresis loop, producing reduced strains and limiting the performance of the device.

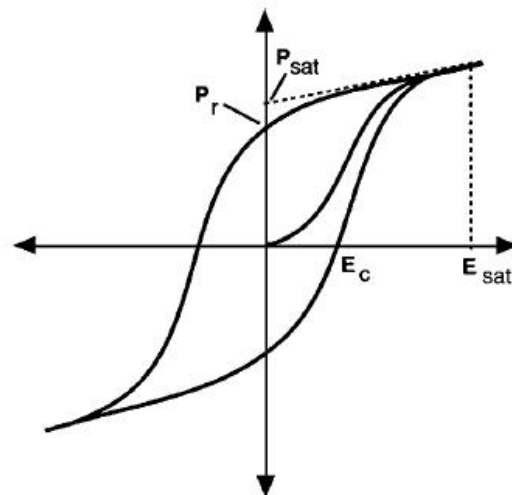


Figure 32. Polarization vs. electric field curve throughout and after poling [30]

To pole the PZT actuators in the scanner, a 40 kV/cm field is produced between the electrodes for approximately 10 minutes, in anticipation of a d_{33} value in the range of 200 pC/N [33]. Increasing the poling temperature to 140 °C can also help to increase the piezo coupling values by up to 20%.

12. Device Packaging

After dicing the device to its final dimensions of 4.75 mm by 5mm, it is packaged in a molded plastic “seat” described in detail in the packaging section. The chip is epoxied into an inset region in the seat and is self-aligned against the edges which are 5 mm by 5mm. A second inset in the seat, shown in figure 39, allows for large deflections of the mass during bending without impacting the package.

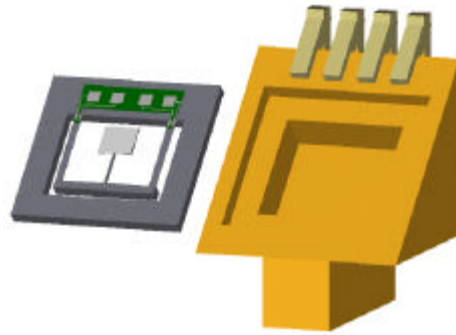


Figure 39. Device and package separated to show insets in package.

The seat includes metal leads to which the external electronics are connected. Contact pads on the device are wire-bonded to these metal leads, as shown in figure 40. A small amount of gel can be placed over the wire bonds to provide insulation.

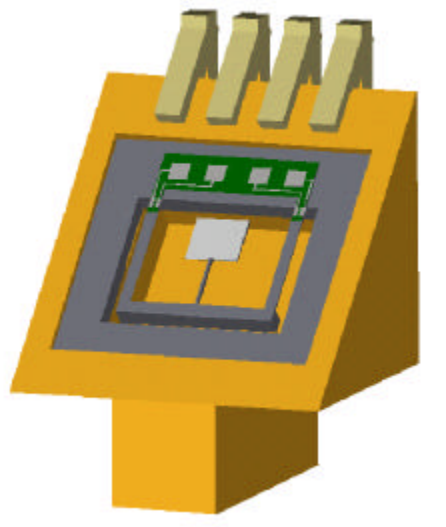


Figure 40. Device epoxied into the package. Wire bonds can be added between the contact pads and lead frame.

13. Conclusion

The design, analysis and fabrication of a novel two-axes optical MEMS scanner have been presented. It is analytically shown that the two scan axes are highly decoupled and free of translational errors. Scan frequencies of 550 Hz and 15.5 kHz are predicted, which are well-separated to produce optimal raster action. PZT actuation has been proposed to excite the two desirable resonance modes of the device. Furthermore, these two resonance frequencies are far enough from the other resonance modes of the device structure. Detailed damping analysis is used to estimate a mechanical scan angle range of $\pm 10^\circ$ at an excitation voltage of less than 20V.

APPENDIX A: MATLAB Code for the Bending and Torsional Dynamics Analysis including List of Symbols

```
% Parameters File for 2-D scanner
% 6.777 Course Project
% Shorya Awtar (Team F-2)
% All dimensions are in SI units unless otherwise stated

% Mirror dimensions (Mass 2)

w_m=900e-6;      % Length and Width of the mirror(also referred
                % to as w2 in the analysis)
t_m=20e-6;      % Thickness of the mirror(also referred to as
                % t2 in the analysis)
vol_m=w_m^2*t_m; % Volume of the mirror in m^3
ro=2330;        % Density of single crystal silicon in kg/m^3
m2=ro*vol_m;    % Mass of the mirror
Im2=m2*w_m^2/12; % Moment of Inertia about in-plane X and Y axes

% Note that the first mass has to be at least 10 times the
second mass

% Intermediate mass (Mass 1) dimensions

w1=3000e-6; % Width of mass1
t1=370e-6; % Thickness of mass1 (which is the same as the wafer
           % thickness)
a1=246e-6; % Length of mass1

voll=w1*t1*b1; % Volume of mass 1
m1=ro*voll;    % Mass 1
Im1=m1*b1^2/12; % Moment of inertia of the intermediate mass
                % about an x axis through its CM

% Dimensions of the cantilever

t=20e-6;      % Thickness of cantilever
l=2250e-6;    % Free length: This is the same as L1 in our
                % derivations
w=200e-6;     % Width of each cantilever

E1=130e9;     % Young's modulus of Silicon
nu=0.278;     % Poisson's Ratio
I1=(2*w)*t^3/12; % Moment of area of the cantilever cross
                % section about x axis
k1=12*E1*I1/l^3 % Bending stiffness of both the cantilevers
                % considered together
```

```

f1=sqrt(k1/m1/4)/2/pi % First order estimate of the first
                        bending mode frequency

% Dimensions of torsion bar

t2=50e-6; % Thickness of the torsion bar
l2=1000e-6; % Length of the torsion bar
w2=50e-6; % Width of the torsion bar
I2=w2*t2^3/12; %Moment of area of torsion bar cross section
                about the x axis
E2=E1;
vol_rod=t2*l2*w2;
m_rod=vol_rod*ro; % Mass of the torsion bar
I_rod=m_rod*l2^2/12; % Moment of Inertia about an x axis passing
                    through its center

k2=12*E2*I2/l2^3 % Bending stiffness of the torsion bar, should
                be 30 times that of the cantilevers

l_m1_m2=w_m/2+l2+b1/2; % Distance between the CGs of m1
                        and m2
lc=l_m1_m2*m2/(m1+m2)-b1/2; % Distance between the CG of
                            composite mass m and point O
m=m1+m2+m_rod; % Composite mass

Ilo=Im2+m2*(w_m/2+l2)^2 + I_rod+m_rod*(l2/2)^2 +
Im1+m1*(b1/2)^2; % Moment of inertia of the
                composite mass about point O
I1c=Ilo-m*lc^2; % Moment of inertia of the
                composite mass about its CG, point C

% Actuator Parameters for bending
c1=4.58e-4;

% Damping terms in bending analysis

b1=1e-6;
b2=1e-12;

% Transfer function between Vin and Theta1 (Bending Analysis)

num=[m*(lc-l/3) b1*(lc-l/3) k1*l/6] * k1*l*c1/2
den=[m*I1c m*b2+b1*I1c m*k1*l^2/3+b1*b2+k1*Ilo-m*k1*l*lc
b1*k1*l^2/3+k1*b2-b1*k1*l*lc+k1*b1*lc^2 k1^2*l^2/12]

```

```

sys1=tf(num,den)

% Natural frequencies of the two bending modes
p=roots(den)/2/pi

% Resulting Quality factors for the two bending modes

Q1=1/2/(real(p(1))/imag(p(1)))
Q2=1/2/(real(p(3))/imag(p(3)))

% Torsion Mode Analysis

It1=m1*w1^2/12; % Mass moment of inertia of first mass about Y
                axis
It2=Im2;      % Mass moment of inertia of second mass about Y axis

% Damping in the torsion mode

b3=1e-13;
b4=1e-14;

Ip2=(w2*t2^3 + t2*w2^3)/12; % Polar moment of area of torsion
                             bar

G=E1/2/(1+nu);
K1=0.5*6*E1*I1*w1^2/l^3    % Torsional stiffness of the beam pair
K2=0.5*G*Ip2/l2          % Torsional stiffness of the torsion
                          bar

c2=K1*c1;
num2=c2*K2;
den2=[It1*It2 It1*b4+It2*b3 It1*K2+It2*(K1+K2)+b3*b4
      b3*K2+b4*(K1+K2) K1*K2];
sys2=tf(num2,den2)
bode(sys2)

% Natural frequencies of the two torsion modes

p2=roots(den2)/2/pi

% Quality factors of the two torsion modes

Q1=1/2/(real(p2(1))/imag(p2(1)))
Q2=1/2/(real(p2(3))/imag(p2(3)))

% End

```

APPENDIX B: Piezoelectric Actuation Calculations

The stiffness matrix, C^E , and the stress-charge coupling matrix, e , are calculated using the compliance matrix, S^E , and strain-charge coupling matrix, d . The stiffness matrix is simply the inverse of the compliance matrix, and the stress-charge coupling matrix is related to the strain-charge coupling matrix as shown in equation (44).

$$e_{ij} = \sum_k^6 d_{ik} C_{kj}^E \quad (44)$$

Values for the compliance matrix and the strain-charge coupling matrix for sol-gel PZT were taken from literature [34].

$$S_E = \begin{bmatrix} 11.5 & -3.7 & -4.8 & 0 & 0 & 0 \\ -3.7 & 11.5 & -4.8 & 0 & 0 & 0 \\ -4.8 & -4.8 & 13.5 & 0 & 0 & 0 \\ 0 & 0 & 0 & 31.9 & 0 & 0 \\ 0 & 0 & 0 & 0 & 31.9 & 0 \\ 0 & 0 & 0 & 0 & 0 & 31.9 \end{bmatrix} * 10^{-12} \text{ m}^2/\text{N}$$

$$d = \begin{bmatrix} 0 & 0 & 0 & 0 & 33 & 0 \\ 0 & 0 & 0 & 33 & 0 & 0 \\ -97 & -97 & 225 & 0 & 0 & 0 \end{bmatrix} * 10^{-12} \text{ m}/\text{V}$$

The resulting stiffness matrix and stress-charge coupling matrix can then be used for calculating the deflection.

$$C_E = \begin{bmatrix} 14.7 & 8.1 & 8.1 & 0 & 0 & 0 \\ 8.1 & 14.7 & 8.1 & 0 & 0 & 0 \\ 8.1 & 8.1 & 13.2 & 0 & 0 & 0 \\ 0 & 0 & 0 & 3.1 & 0 & 0 \\ 0 & 0 & 0 & 0 & 3.1 & 0 \\ 0 & 0 & 0 & 0 & 0 & 3.1 \end{bmatrix} * 10^{10} \text{ N}/\text{m}^2$$

$$e = \begin{bmatrix} 0 & 0 & 0 & 0 & 10.3 & 0 \\ 0 & 0 & 0 & 10.3 & 0 & 0 \\ -3.9 & -3.9 & 13.9 & 0 & 0 & 0 \end{bmatrix} \text{ C}/\text{m}^2$$

APPENDIX C: Process for Scanner Fabrication

| Step | Process Description |
|----------------------|--|
| Starting Material | SOI wafer: 350 μm handle wafer, .5 μm SiO ₂ , 40 μm Si |
| 1. Clean | Standard RCA clean |
| 2. Oxide* | Deposit 1 μm SiO ₂ with CVD |
| 3. Photolithography* | Mask 1 (Backside) |
| 4. Etch* | DRIE etch through backside of wafer up to SiO ₂ etch stop |
| 5. Strip* | Strip photoresist |
| 6. Photolithography | Mask 2 (Stiffener) |
| 7. Etch | DRIE etch 20 μm to create stiffener |
| 8. Strip | Strip photoresist |
| 9. Oxide | Deposit 250 nm SiO ₂ with CVD |
| 10. Photolithography | Mask 3 (Oxide1) |
| 11. Etch | RIE etch oxide using CF ₄ /H ₂ |
| 12. Strip | Strip photoresist |
| 13. Photolithography | Mask 4 (Electrodes1) |
| 14. Metal | Evaporate 100 \AA Pt, 1000 \AA Ti |
| 15. Strip | Strip photoresist |
| 16. PZT | Spin on sol-gel PZT and dry (repeat to 1 μm) |
| 17. Photolithography | Mask 5 (PZT) |
| 18. Etch | BOE etch PZT (10HN ₄ F:1HF) ~.13 $\mu\text{m}/\text{min}$ |
| 19. Etch | Etch PZT residue (2HCL:H ₂ O) |
| 20. Strip | Strip photoresist |
| 21. Oxide | Deposit 250 nm SiO ₂ with CVD |
| 22. Photolithography | Mask 6 (Oxide2) |
| 23. Etch | RIE etch oxide using CF ₄ /H ₂ |
| 24. Strip | Strip photoresist |
| 25. Photolithography | Mask 7 (Electrodes2) |
| 26. Metal | Evaporate 100 \AA Pt, 1000 \AA Ti |
| 27. Strip | Strip photoresist |
| 28. Photolithography | Mask 8 (Mirror) |
| 26. Metal | Evaporate 100 \AA Cr, 1000 \AA Al |
| 27. Strip | Strip photoresist |
| 28. Etch* | RIE etch oxide using CF ₄ /H ₂ |
| 29. Photolithography | Mask 9 (Space) |
| 30. Etch | DRIE etch surface to free mirror and beams (20 μm) |
| 31. Strip | Strip photoresist |
| 32. Pole | Apply 40 kV/cm @ 140 C for 10 min through electrodes |

**Backside process*

Reference

1. W. Drexler, U. Morgner, R. K. Ghanta, F.X. Kartner, J. S. Schuman, and J. G. Fujimoto, "Ultrahigh-Resolution Ophthalmic Optical Coherence Tomography", *Nature Medicine*, Vol. 7, No. 4, pp. 502-507, April 2001.
2. US 4421381, T. Ueda et al, "Mechanical Vibrating Element", Yokogawa Hokushin Electric Corp.
3. US 6044705, A.P. Neukermans et al, "Micromachined Members coupled for relative rotation by torsion bars", Xros Inc.
4. US 6245590, D.W. Wine et al, "Frequency tunable resonant scanner and method of making", Microvision Inc.
5. US 6201231, M. Regensburger et al, "Testing system for Measurement and Optimising target tracking systems", Diehl Stiftung
6. US 5920417, M.D. Johnson, "Microelectromechanical Television Scanning Device and Method for making the same", Medcam Inc.
7. US 6285489, M.P. Helsei, "Frequency Tunable Resonant Scanner with Auxiliary arms", Microvision Inc.
8. US 5661591, T.H Lin et al, "Optical Switch having an Analog Beam for Steering Light", Texas Instruments Inc.
9. US 5165279, B. L. Norling et al, "Monolithic Accelerometer with Flexurally mounted Force Transducer", Sundstrand Corporation
10. US 5097354, H. Goto, "Beam Scanner", Omron Corporation
11. US 5828051, H. Goto, "Optical Scanner and Bar Code reader employing the same", Omron Corporation
12. M. Ikeda, H.Goto, H. Totani, M. Sakata, T. Yada, "Two-dimensional miniature optical-scanning sensor with silicon micro-machined scanning mirror", *SPIE Vol. 3008*, 1997
13. Y. Ohtuka, H. Nishikawa, T. Koumura, T. Hattori, "2-dimensional optical scanner applying a torsional resonator with 2 degrees of freedom", *Micro Electro Mechanical Systems, 1995, MEMS '95, Proceedings. IEEE*, 1995
14. S. Kurth, R. Hahn, C. Kaufmann, K. Kehr, J. Mehner, U. Wollmann, W. Dotzel, T. Gessner, "Silicon mirrors and micromirror arrays for spatial laser beam modulation", *Sensors and Actuators A66*, 1998
15. D.T. Neilson, R. Ryf, "Scalable micro mechanical optical crossconnects", *Lasers and Electro-Optics Society 2000 Annual Meeting. LEOS 2000. 13th Annual Meeting. IEEE*, Volume: 1, 2000, Page(s): 48 -49 vol.1
16. G.-D.J. Su, H. Toshiyoshi, M.C. Wu, "Surface-micromachined 2-D optical scanners with high-performance single-crystalline silicon micromirrors", *IEEE Photonics Technology Letters*, Volume: 13 Issue: 6, June 2001, Page(s): 606 -608
17. M. H. Kiang, O. Solgaard, K. Y. Lau, R.S. Muller, "Polysilicon optical microscanners for laser scanning displays", *Sensors and Actuators, A70*, 1998, Pages 195-199.
18. R.A. Conant, J. Nee, M. Hart, O. Solgaard, K.Y. Lou, R.S. Muller, "Robustness and reliability of micromachined scanning mirrors", *MOEMS'99*
19. P.M. Gerhart and R.J. Gross, "Fundamentals of Fluid Mechanics", Addison-Wesley, 1992, pp. 608.

20. O. Solgaard, Talk on "Optical MEMS Switches", 10/16/00
http://klamath.stanford.edu/ors/FALL2000/TALKS/olav_omems.pdf
21. A. Garnier, T. Bourouina, E. Orsier, T. Masuzawa, H. Fujita, T. Hiramoto and J.C. Peuzin, "A Fast, Robust and Simple 2-D Micro-Optical Scanner Based on Contactless Magnetostrictive Actuation". IEEE MEMS 2000, 13th Conference on MicroElectroMechanical Systems, January 23-27 2000, Miyazaki, Japan pp.715-720
22. E. Thielicke and E. Obermeier, "Microactuators and their technologies", *Mechatronics* 10, 2000, pp. 431 – 455.
23. H. Toshiyoshi, W. Piyawattanametha, C.T. Chan and M.C. Wu, "Linearization of Electrostatically Actuated Surface Micromachined 2D Optical Scanner", IEEE/ASME J. Microelectromech. Syst. volume 10, June 2001.
24. R.A. Conant and R. S. Muller, "Cyclic Fatigue Testing of Surface-Micromachined Thermal Actuators", ASME International Mechanical Engineering Congress and Exposition, November 15-20, 1998, Anaheim, CA, DSC-Vol. 66, pp. 273-277.
25. R.A. Conant, J.T. Nee, K.Y. Lau and R.S. Muller, "A Flat High-Frequency Scanning Micromirror", Hilton Head 2000 Conference, Hilton Head, South Carolina, June 4-8, 2000.
26. M. Madou, "Miniaturization Science", MEMS Workshop,
<http://www.biomems.net/Classes/MEMSWorkshop/MEMS%20Class%209.pdf>
27. W.D. Callister, "Materials Science and Engineering: An Introduction", John Wiley & Sons, 1999.
28. C. L. Muhlstein, E. A. Stach and R. O. Ritchie, "Mechanism of Fatigue in Micron-Scale Films of Polycrystalline Silicon for Microelectromechanical Systems", *Applied Physics Letters*, vol. 80 (9), Mar. 4, 2002, pp.1532-1534.
29. <http://www.bco-technologies.com/proservices/substrate/>
30. D. L. Polla, L. F. Francis, "Processing and Characterization of Piezoelectric Materials and Integration Into Microelectromechanical Systems," *Annual Review of Materials Science* 28:563-597 1998
31. Y. Chen and I-W. Chen, "Temperature-Time-Texture Transition of Pb(Zr_{1-x}Ti_x)O₃ Thin Films I. The Role of Pb-rich Intermediate Phases," *J. Amer. Ceram. Soc.* 77 [9] 2232-36 (1994).
32. L. P. Wang, R. Wolf, Q. Zhou, S. Trolier-McKinstry, R. J. Davis, "Wet-etch Patterning of Lead Zirconate Titanate (PZT) Thick Films for Microelectromechanical Systems (MEMS) Applications," *Mat. Res. Soc. Symp. Proc.* 657:EE5.39.1-EE5.39.6 2001
33. K. Lefki, G. J. M. Dormans, "Measurement of Piezoelectric Coefficients of Ferroelectric Thin Films," *J. Appl. Phys.* 76:1764-67 1994
34. <http://www.ohiocae.com/piezo-paper.htm>